

# Effect of grain shape on quasi-static fluid-fluid displacement in porous media

Zhongzheng Wang<sup>1,2</sup>, Jean-Michel Pereira<sup>2</sup>, and Yixiang Gan<sup>1,3</sup>

<sup>1</sup>School of Civil Engineering, The University of Sydney, NSW 2006, Australia.

<sup>2</sup>Navier, Ecole des Ponts, Univ Gustave Eiffel, CNRS, Marne-la-Vallée, France.

<sup>3</sup>The University of Sydney Nano Institute (Sydney Nano), The University of Sydney, NSW 2006, Australia

## Key Points:

- A novel pore network model algorithm is developed to probe the effect of grain shape on multiphase displacement in porous media.
- Systematic simulations are conducted using the proposed algorithm across a wide range of wetting conditions and particle shapes.
- Through analyzing various metrics during displacement, the results highlight the profound influence of particle shape on multiphase flow.

---

Corresponding author: Yixiang Gan, [yixiang.gan@sydney.edu.au](mailto:yixiang.gan@sydney.edu.au)

## Abstract

We study how grain shapes impact multiphase flow in porous media in the quasi-static regime. An extended pore-network model with consideration of menisci pinning at sharp edges of grains is presented. Our results show that the effective contact angle distribution during displacement widens as the grain becomes more angular, which consequently modifies the macroscopic fluid invasion morphology. By analyzing various characteristic metrics during displacement, including capillary pressure signal, Haines jump size distribution, and fractal dimension, our results highlight the profound influence of particle shape on the multiphase flow.

## 1 Introduction

Fluid-fluid displacement in porous media is a common phenomenon encountered in a wide range of natural and industrial processes, such as water infiltration into soil (Lipiec, Kuś, Słowińska-Jurkiewicz, & Nosalewicz, 2006), carbon sequestration (Matter et al., 2016; Szulczewski, MacMinn, Herzog, & Juanes, 2012), enhanced oil recovery (M. Blunt, Fayers, & Orr, 1993; Lake & of Petroleum Engineers (U.S.), 1986), and remediation of contamination in aquifer systems (Nadim, Hoag, Liu, Carley, & Zack, 2000). As indicated by the pioneering works by Lenormand et al (Lenormand, Touboul, & Zarcone, 1988; Lenormand & Zarcone, 1989), the multiphase displacement patterns strongly depend on the capillary number (i.e., relative strength of viscous force to capillary force) and the viscosity ratio of the two fluids, and a phase diagram including capillary fingering, viscous fingering, and stable displacement was presented. Since then, extensive efforts have been devoted to further investigation of how fluid properties, flow conditions, and topological characteristics of the porous media modify the invasion morphology (Armstrong, Georgiadis, Ott, Klemen, & Berg, 2014; Holtzman, 2016; Hu, Lan, Wei, & Chen, 2019; Ju, Gong, Chang, & Sun, 2020; Rabbani et al., 2018; Wang, Chauhan, Pereira, & Gan, 2019; Xu, Ok, Xiao, Neeves, & Yin, 2014; Yortsos, Xu, & Salin, 1997). Specifically, both numerical and experimental works have revealed the profound influence of wettability (i.e., contact angle) in two phase flows (Cieplak & Robbins, 1990; Holtzman & Segre, 2015; Jung et al., 2016; Primkulov et al., 2018; Ran, Jiamin, Zhibing, Yi-Feng, & Tetsu, 2018; Trojer, Szulczewski, & Juanes, 2015; Wang et al., 2019; Wang, Pereira, & Gan, 2020; Zhao, MacMinn, & Juanes, 2016). However, the effective contact angle, as one of the key controlling factors, is often unknown prior to the displacement process due to the complex geometry of pore space. Even for chemically homogeneous porous media, a wide distribution of contact angles have been observed due to roughness and pinning of menisci at sharp edges (AlRatrou, Blunt, & Bijeljic, 2018; M. J. Blunt, Alhosani, Lin, Scanziani, & Bijeljic, 2021; M. J. Blunt, Lin, Akai, & Bijeljic, 2019). Therefore, it is important to understand how particle shape affects the effective contact angles, which can consequently alter the pore-scale instability events and macroscopic invasion morphology (AlRatrou et al., 2018; Cieplak & Robbins, 1990; Geistlinger & Zulfiqar, n.d.; Holtzman & Segre, 2015; Zulfiqar et al., n.d.).

In the quasi-static regime of multiphase flow where capillary force dominates the displacement, various numerical approaches have been developed to supplement experiments, including Navier-Stokes equation solvers and pore-network models. The methods of the latter category have been successfully applied in investigation of macroscopic invasion patterns due to significantly less computational cost (M. J. Blunt, 1998, 2001; Cieplak & Robbins, 1988, 1990; Holtzman, 2016; Holtzman & Segre, 2015; Hu et al., 2019; Primkulov et al., 2018). A subclass of pore-network models, the interface tracking algorithm, initially proposed by Cieplak and Robbins (Cieplak & Robbins, 1988, 1990) and recently extended by Primkulov et al. (Primkulov et al., 2018) for consideration of corner flow, has been found successful in reproducing multiphase displacement experiments in Hele-Shaw cells (Holtzman, 2016; Holtzman & Segre, 2015; Ran et al., 2018; Trojer et al., 2015; Zhao et al., 2016). This method captures the pore-scale invasion mechanisms

by taking into account the local pore geometry, including the cooperative pore-filling event, which stabilizes the invasion during imbibition (Cieplak & Robbins, 1988, 1990; Holtzman & Segre, 2015). However, up to now, this type of pore-network models is applicable to perfectly spherical particles, whereas grains with irregular shapes are prevalent in natural systems such as sand packs, and solid walls characterized by surface roughness or sharp edges due to manufacture limitations are encountered in microfluidics. These non-smooth surfaces can often lead to pinning of menisci during displacement process, which results in apparent contact angles deviating from the intrinsic one, altering the capillary resistance at local pore/throat.

Here, we develop an extended pore-network model (called EPONM) to probe the effect of particle shape on quasi-static fluid-fluid displacement. The model incorporates the explicit determination of basic pore-scale instabilities based on the work of Cieplak and Robbins (Cieplak & Robbins, 1988, 1990). It also includes the volume capacitance model (Furuberg, Måløy, & Feder, 1996; Måløy, Furuberg, Feder, & Jøssang, 1992), which allows us to capture both the evolution of capillary pressure signal and sizes of Haines jumps. Different from the original algorithm where the volume capacitance is a prescribed constant (Furuberg et al., 1996; Måløy et al., 1992), it is calculated based on local pore geometries without extra assumptions. More importantly, the sharp edge pinning effect is added to consider the pinning of the menisci (Gibbs, 1961; Oliver, Huh, & Mason, 1977). Our results for different grain shapes indicate that increase in angularity leads to wider distribution of contact angles, which explains the observed greater fluctuations in capillary pressure. Besides, it is found that comparing with more spherical particles, the mean capillary pressure for angular grains is greater in drainage whereas smaller in imbibition. We quantify and analyze the correlation between grain shape and size distribution of Haines jumps, interfacial length, and fractal dimension across a wide range of wetting conditions. The implications of our findings are then discussed.

## 2 Extended Pore-Network Model

To model the 2D flow patterns observed in Hele-Shaw cells filled with vertical posts (Hu et al., 2019; Primkulov et al., 2018; Trojer et al., 2015; Zhao et al., 2016) with controlled particle shapes, the porous medium is represented by polygons (instead of circles in past studies) placed on two-dimensional triangular lattice. The invading fluid is injected from the center of the simulation domain. Based on a purely geometrical extension of Young-Dupre equation (Gibbs, 1961; Oliver et al., 1977), the equilibrium state of apparent (or effective) contact angle  $\theta$  at the triple line follows:

$$\theta_0 \leq \theta \leq \theta_0 + (180^\circ - \alpha), \quad (1)$$

where  $\theta_0$  and  $\alpha$  are the intrinsic contact angle and the angle subtended by the two surfaces forming the edge, respectively (Fig. 1(A)). Since in this work the focus is placed on the regime of quasi-static displacement, the advancement of liquid front is governed by capillary force, and the viscous effect is ignored.

In the framework of interface tracking algorithm, the menisci move forward through two types of advancements: (1) pressure-driven events and (2) spontaneous events (relaxation). With a constant injection velocity boundary condition, the capillary pressure builds up accompanied by change in shapes in menisci, until either the meniscus jumps towards the next mesh point due to the local contact angle being greater than the upper bound according to Eqn. 1 (*unpin* event), or the meniscus touches other grain, forming two new menisci (*touch* event). After each pressure-driven event, the newly invaded area is subtracted from the total volume capacitance (Furuberg et al., 1996; Måløy et al., 1992) (area between red and blue-dashed lines in Fig. 1(D)), from which the capillary pressure within the invading fluid is updated according to the remaining volume capacitance. Then, potential *overlap* event and further advancement events including *unpin* and/or *touch* are checked and executed. This process is carried out until the small-

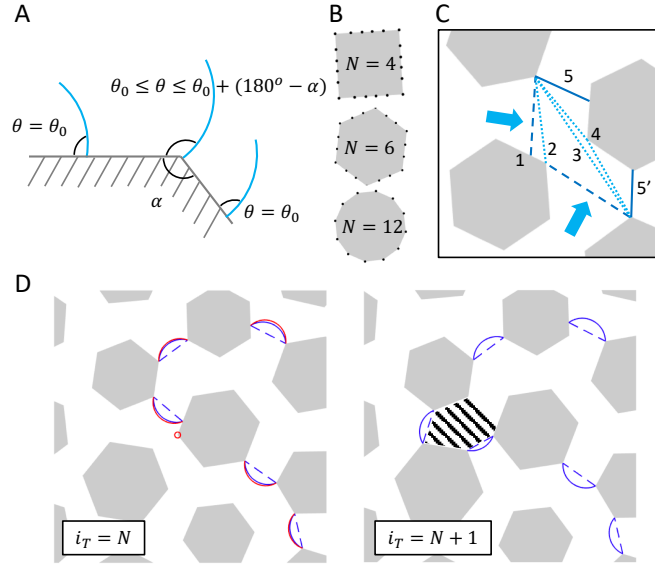


**Figure 1.** (A) Pinning of menisci at corners leads to greater apparent contact angle. (B) Investigated grain shapes in this work with different number of edges  $N$ . The black dots represent the mesh points. (C) Schematic showing different invasion types.  $\{1-2, 2-3, 3-4, 4-5(5')\}$  correspond to  $\{\text{unpin, overlap, touch, unpin}\}$  events, respectively. Blue arrows mark the movement direction of menisci. (D) Snapshots of invasion morphology at two consecutive iterations. Blue solid lines represent menisci after relaxation of previous step. Red solid lines represent menisci at the critical state (in this case an unpin event marked by the red circle will take place). The shaded area is invaded, accompanied by retraction of menisci from red lines at  $i_T = N$  to blue lines at  $i_T = N + 1$ .

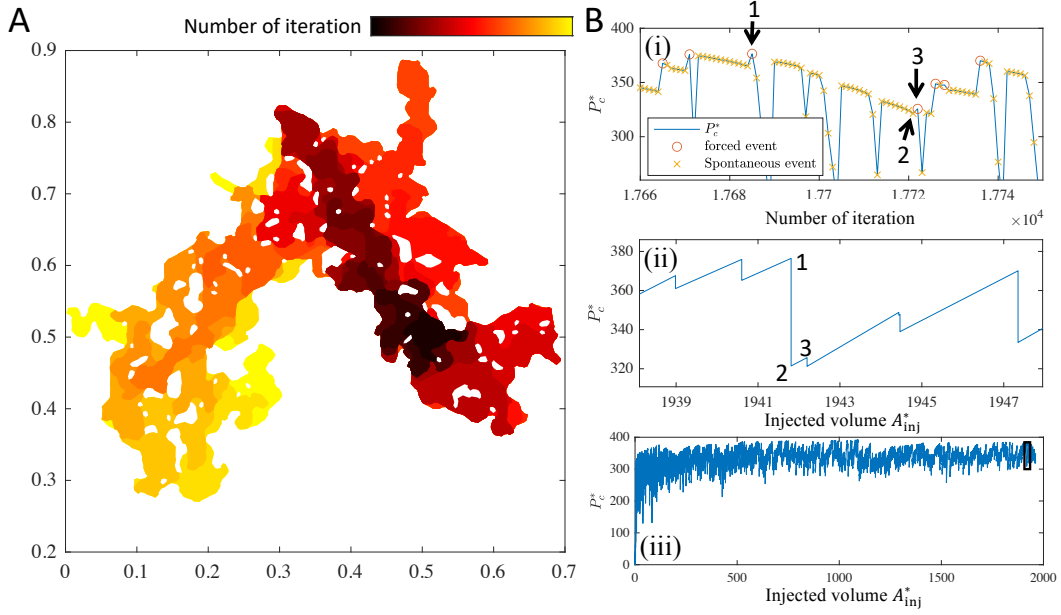


**Figure 2.** (A) Invasion morphology with hexagon grains (Number of edges  $N = 6$ ) and  $\theta_0 = 120^\circ$ . The color represents displacement patterns at different number of iteration. (B) Process of capillary pressure signal: (i) Evolution of dimensionless capillary pressure calculated as the local curvature  $P_c^* = 1/r^*$  in terms of number of iteration. Red circle marks the critical capillary pressure, where the pressure-driven advancement occurs. Yellow crosses represent the consequent spontaneous events (relaxation). (ii) Conversion from the iteration step into time expressed in terms of injected fluid area  $A_{inj}^*$  which is normalized by the average pore area. The time for Haines jump is regarded as instantaneous, i.e., only the start and end of  $P_c^*$  are “felt” at the inlet. The  $P_c^*$  values at same invasion progress are marked by the same number in (i) and (ii). (iii) Capillary pressure signal during the whole simulation. The black box is (ii).

est capillary resistance at the invasion front is greater than the remaining capillary pressure within the invading fluid. Note that after each time step, trapping is checked and all menisci that belong to trapped regions are deactivated to prevent any further movement. Fig. 1(C) shows the schematic of several advancement steps initialized by a pressure-driven *unpin* event. Fig. 1(D) shows local snapshot of invasion morphology at two consecutive time steps.

To investigate the effect of particle shapes, squares, hexagons, and dodecagons were chosen as representative grains with decreasing angularity (Fig. 1(B)). The rectangular simulation domain contains in total 7520 particles with constant porosity of  $0.5912 \pm 0.0005$ . Disorder is introduced by (i) inducing 10 percent variation in particle size with a uniform distribution and (ii) random rotation of particles in  $[0^\circ, 360^\circ)$ . The capillary pressure signal, total injected fluid volume (area in 2D), and size of Haines jump are recorded at each iteration, until the invasion front reaches the boundary. Simulations were carried out for each particle shape with five randomly generated porous media under contact angles ranging from  $45^\circ$  to  $165^\circ$  with  $15^\circ$  increment.

A typical evolution of the invasion front until breakthrough for hexagonal grains with an intrinsic contact angle of  $\theta_0 = 120^\circ$  is shown in Fig. 2(A). Crimson represents the initial stage whereas yellow indicates the late times. The displacement pattern contains rather ramified structures with significant trapping, which represents the capillary

fingering in drainage. Fig. 2(B-i) shows the evolution of the dimensionless capillary pressure (curvature of menisci) associated with the pressure-driven events (red circle) and subsequent spontaneous events (yellow cross). Clearly, multiple spontaneous events can take place following a pressure-driven event, which is a manifestation of a Haines jump. In the limit of vanishing capillary number, Haines jump can be regarded as effectively instantaneous compared with the speed of fluid injection at the inlet. Thus, after conversion from iteration step into time, which is expressed as volume of injected area normalized by the average pore area, Fig. 2(B-ii) shows the pressure signal as a function of  $A_{\text{inj}}^*$ . The  $P_c^*$  values at same invasion progress are marked by the same number in Fig. 2(B-i) and Fig. 2(B-ii). Specifically, the processes marked by (1-2) and (2-3) represent a fast Haines jump accompanied by drop in pressure, and slow injection of invading fluid until the next critical  $P_c^*$  is reached, respectively. Fig. 2(B-iii) shows  $P_c^*$  signal for the whole simulation. Similar pressure signal signatures in a stick-slip manner have been observed in experiments at quasi-static condition (Furuberg et al., 1996; Måløy et al., 1992; Moura, Måløy, Flekkøy, & Toussaint, 2020).

### 3 Results and Discussion

The phase diagram of the displacement patterns across a wide range of contact angles for different particle shapes is shown in Fig. 3(A). The invasion morphology for medium with dodecagons at  $\theta_0 = 45^\circ$  is compact with rather smooth front. This hexagonal shape is a direct result of the grain placement in the triangular lattice, which has been observed in previous study (Holtzman, 2016). However, with increase in angularity, despite the displacement pattern is still relatively stable without trapping, the invasion front becomes more irregular, indicating a shift of the dominance of local pore geometry from lattice structure towards grain shape. The results at  $\theta_0 = 60^\circ$  demonstrate similar trend, with trapping events starting to occur for angular grains. With the increase of  $\theta_0$ , the displacement patterns experience a transition from compact displacement to capillary fingering. The distribution of the normalized throat size  $L_t^*$ , calculated as the shortest distance between adjacent grains divided by the throat size of the volume-equivalent spheres, is shown in Fig. 3(B). Although the media have similar grain size distribution (10 percent variation with uniform distribution) and arrangement (placed on triangular lattice), the  $L_t^*$  distribution varies drastically for different grain shapes, with wider span for more angular grains, similar to the effect from increasing topological disorder (Wang et al., 2019). Another influence of particle shape is the smaller average throat size as angularity increases, despite almost constant porosity. For media filled with dodecagons, the average throat size is close to 1, i.e., the average throat size is similar to media with perfect spheres, which implies that the shape of dodecagons can be regarded as very close to spherical particles. Fig. 3(C) shows the effective contact angle distribution  $\theta$  for the case with an intrinsic contact angle  $\theta_0 = 120^\circ$ . Due to the sharp edge pinning effect, the distribution narrows for grains with decreasing angularity. In the case of perfect spheres, one can expect a single value of  $\theta = \theta_0$  according to Eqn. (1). Therefore, Fig. 3(B) and Fig. 3(C) summarize the important influences of particle angularity on pore geometry features and contact angle distribution, which will consequently impact the capillary pressure signal and invasion morphology.

#### 3.1 Capillary Pressure Signal

As indicated in Fig. 4(A), the evolution of dimensionless capillary pressure  $P_c^*$  shows larger fluctuations for media with squares compared with more spherical grains (dodecagons), implying greater randomness in local capillary resistance. At the same time, larger mean value is observed with increasing  $\theta_0$ , which is a direct result from greater curvature of menisci. The distribution of  $P_{\text{start}}^*$ , the avalanches starting pressure, can also be directly obtained from the simulation (Fig. 4(B)), where  $P_{\text{start}}^*$  is the capillary pressure at pressure-driven event (red circle in Fig. 2(B-i)). For experiments conducted using spherical glass

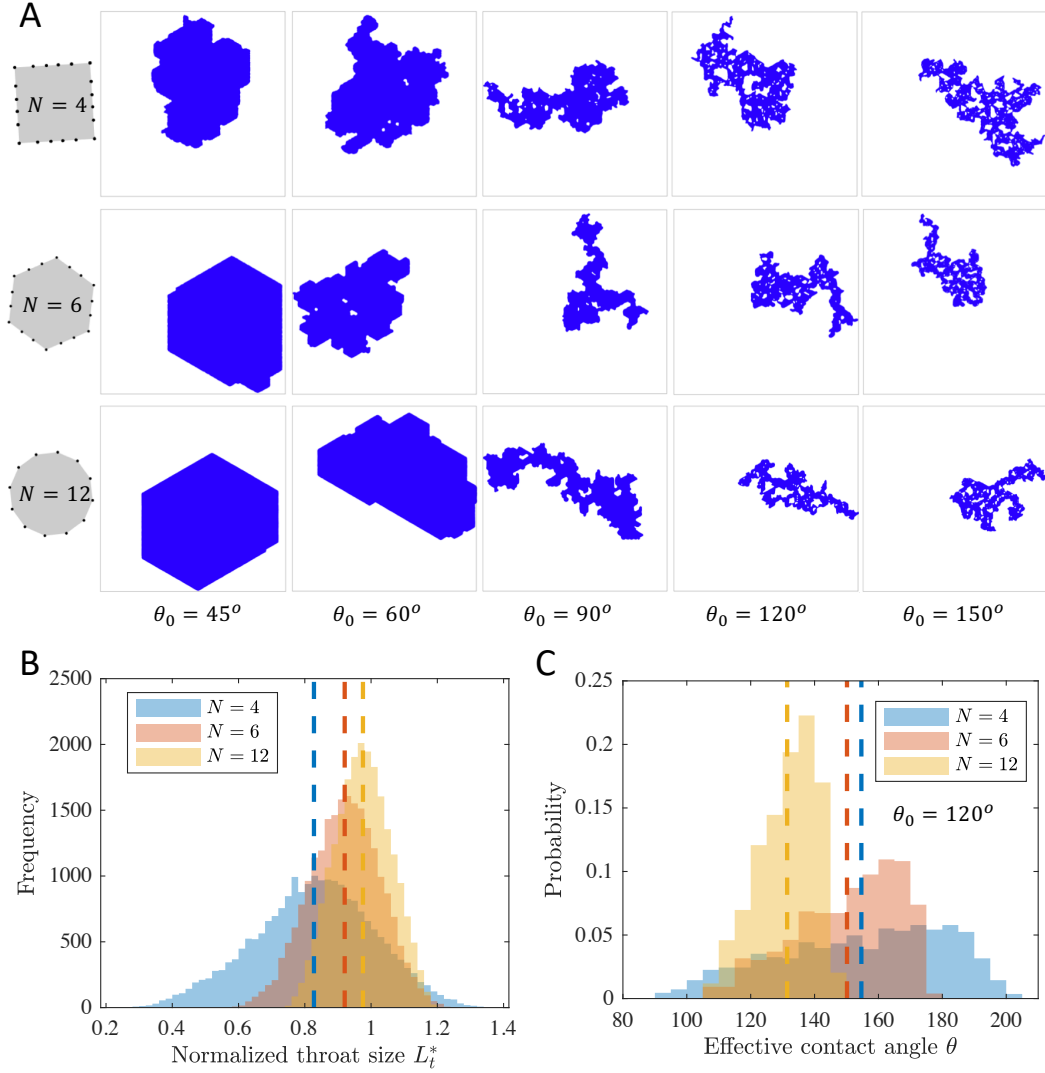


**Figure 3.** (A) Displacement patterns at the end of the simulation for different wettability conditions and grain shapes. Blue color represents the invading fluid injected from the center of domain. The simulation ends when the invading fluid reaches the boundary. (B) Distribution of normalized throat size for a typical set of porous media of different grain shapes, calculated as the shortest distance between adjacent grains divided by the throat size of volume equivalent spheres. (C) Contact angle distribution of one typical simulation with an intrinsic contact angle  $\theta_0 = 120^\circ$  for different grain shapes. The dashed lines marks the average value for the corresponding data.



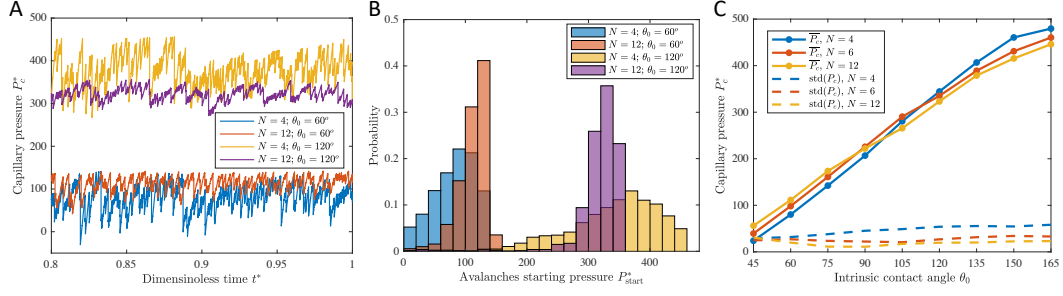


**Figure 4.** (A) Capillary pressure signals  $P_c^*$  for media with squares and dodecagons at  $\theta_0 = 60^\circ$  and  $\theta_0 = 120^\circ$ . Only last 20 percent of invasion is plotted for visualization purpose. (B) Corresponding avalanches starting pressure  $P_{start}^*$  distribution for cases in (A), which is the  $P_c^*$  at pressure-driven event (red circle in Fig. 2(B-i)). (C) Mean and standard deviation in  $P_c^*$  for all grain shapes and wettability conditions. Values are calculated from five individual simulations.

beads in drainage,  $P_{start}^*$  is found to distribute within a relatively narrow region (Furuberg et al., 1996; Måløy et al., 1992; Moura et al., 2020). The  $P_{start}^*$  distribution is linked to the total volume capacitance stored in all active menisci (Furuberg et al., 1996), which reflects the characteristics of pore geometry. For spherical grains with given packing structure, the capillary resistance is distinct between “pore” and “throat”, leading to the fact that the avalanches are likely to initialize (and finish) at same location and consequently similar  $P_{start}^*$ . As the shape of particle becomes more angular, the distribution of  $P_{start}^*$  widens as a result of increased impact from random orientations of grains and pinning of menisci, which is clearly demonstrated in Fig. 4(B). Fig. 4(C) depicts the mean and standard deviation of  $P_c^*$  for all grain shapes and wettability with each value calculated from five individual simulations. As expected, the average capillary pressure increases with increasing contact angle, and the fluctuations in capillary pressure are found to be larger for more angular grains across all wetting conditions. Interestingly,  $\bar{P}_c^*$  is greater (smaller) for angular grains in drainage (imbibition) conditions, with a crossover at around  $\theta_0 \approx 90^\circ$ . This implies that the capillary pressure signal is more sensitive to variations in wettability for angular grains.

### 3.2 Haines Jumps and Patterns Characteristics

The size of Haines jump can be obtained as the area filled between two pressure-driven event (shaded area in Fig. 1(D)). Fast filling events of single and multi pores are observed during the displacement process. Both the cumulative pressure jump sizes and intervals distributions during drainage experiments have been found to follow an exponential law (Furuberg et al., 1996; Måløy et al., 1992), which is consistent with the simulation results (inset in Fig. 5A). The time interval between two jumps is expressed as the injected area of invading fluid, and the area of invading fluid is expressed in terms of number of average pore volume, calculated as the total pore space divided by the number of pores. Note that the cumulative intervals distribution is shifted upwards by 0.5 for visualization purpose. The power exponent  $\beta$ , which is regarded as a signature of the displacement process (Furuberg et al., 1996; Måløy et al., 1992), is plotted for different grain shapes and wetting conditions (Fig. 5A). It can be seen that  $\beta$  increases with the intrinsic contact angle, reaching a plateau at around  $\theta_0 = 120^\circ$ . Also, in general, the angularity positively correlates with the power exponent. The power exponent  $\beta$  from Måløy et al. (Måløy et al., 1992) in drainage experiment with glass beads is added as black-dashed line for comparison. Since the contact angle was not reported, it is assumed



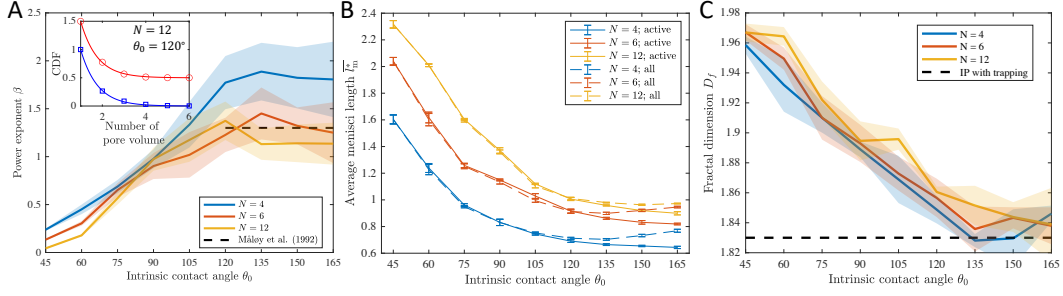


**Figure 5.** (A) Power exponent  $\beta$  for different grain shapes and wetting conditions. The black-dashed line is from Måløy et al. (Måløy et al., 1992) in drainage experiment with glass beads (since the contact angle is not reported, it is assumed that  $\theta_0 > 120^\circ$ ). Inset: cumulative Haines jump sizes (blue squares) and intervals (red circles) distribution for a typical simulation at  $N = 12$  with  $\theta_0 = 120^\circ$ . The intervals distribution is shifted by 0.5 for visualization purpose. Lines represent exponential fitting with 1.29 and 1.30 for jump sizes and interval sizes, respectively. (B) The normalized average meniscus width  $\bar{l}_m^*$  as a function of intrinsic contact angle. Solid (dashed) lines represent values calculated from all (active) menisci. (C) Fractal dimension calculated using box counting method as a function of intrinsic contact angle, with shaded area showing the standard deviation of five simulations.

that  $\theta_0 > 120^\circ$ . Their value of  $\beta$  is close to the less angular grains (hexagons and dodecagons), which is consistent with the fact that glass beads are comparatively round and smooth.

The average meniscus width  $\bar{l}_m^*$ , normalized by the throat size of porous medium of same porosity filled with mono-dispersed spheres, can reveal the preferential distribution of fluid-fluid interfaces with the tendency of minimization of free energy. Fig. 5(B) shows  $\bar{l}_m^*$  as a function of intrinsic contact angle for different angularities with or without consideration of menisci belonging to trapped region. For all active menisci (solid lines),  $\bar{l}_m^*$  decreases with increasing  $\theta_0$ , reflecting stronger stability of pinned meniscus at small throat. Besides, despite constant porosity for all simulations, the average meniscus size is found to be smaller in angular grains as a result of (i) wider distribution of throat sizes (Fig. 3(B)), and (ii) greater capacity of pinning (upper bound in Eqn. (1)) as the local corner becomes sharper, leading to wider distribution of effective contact angles (Fig. 3(C)). If both active and inactive menisci are considered, however, a non-monotonic relationship is observed. This is a result of incompressibility of the trapped ganglia that prevent the menisci from further advancement and ultimately being pinned at narrower throats. Due to increased amount of trapping at larger contact angle (see Fig. 3(A)), this effect becomes significant at extreme non-wetting condition that leads to increase in  $\bar{l}_m^*$ . This also implies that the capillary pressure within the trapped ganglia could be lower than the capillary pressure signal measured at the inlet.

To quantify the displacement patterns, the fractal dimension  $D_f$ , as a measurement of the degree to which a pattern fills space, is calculated using box counting method. Fig. 5(C) demonstrates the transition from stable displacement with a  $D_f$  of around 1.96 towards the regime of capillary fingering with  $D_f \approx 1.84$ , which is consistent with previously documented values of 1.96 and 1.83 for compact growth and invasion percolation, respectively (M. J. Blunt, 2017; Lenormand & Zarcane, 1989; Primkulov et al., 2018; Trojer et al., 2015; Wilkinson & Willemsen, 1983; Zhao et al., 2016). Furthermore, in spite of considerable variability, an early transition towards capillary fingering, i.e., smaller  $D_f$  at the same  $\theta_0$ , can be observed for grains with greater angularity, which confirms the

qualitative observation in the displacement patterns in Fig.3(A). This could be partially explained by, apart from the variation in local pore structure, the increase of average effective contact angles in angular grains assemblies due to sharp edge pinning effect, which is evident in Fig. 3(C).

In this study, though we considered simplified particle shapes (regular polygons), more general and complex shapes can be easily implemented by changing the coordinates of grain vertices and updating the local corner angles accordingly. Furthermore, it is also possible to consider the viscous effect by incorporating, for example, the recently proposed moving capacitor model (Primkulov et al., 2019).

## 4 Conclusions

In conclusion, we presented an extended pore-network model (EPONM) to probe the effect of grain shapes on quasi-static fluid-fluid displacement in porous media. The model incorporates the mechanisms of pore-scale instabilities (Cieplak & Robbins, 1988, 1990), volume capacitance model (Furuberg et al., 1996; Måløy et al., 1992), and sharp edge pinning effect (Gibbs, 1961; Oliver et al., 1977). This allows us to reproduce the multiphase flow patterns across a wide range of wetting conditions for different grain shapes. The algorithm is in theory applicable to porous media with arbitrary grain shape, offering a rigorous approach for investigation of how topological features modify the multiphase displacement in porous media.

At the pore scale, increase in grain angularity not only introduces another degree of heterogeneity in pore geometry apart from grain size, but also extends the effect of menisci pinning at corners. This is directly reflected by the amplified fluctuations in pressure signals (Fig. 4(A)) and the widened contact angle distributions (Fig. 3(C)) for more angular grains. Macroscopically, an earlier transition from stable displacement towards the regime of capillary fingering is observed both qualitatively from the invasion morphology (Fig. 3(A)) and quantitatively as indicated by the fractal dimension (Fig. 5(C)). Various characteristic metrics have been calculated for comparison with past experimental works, including the distribution of avalanches starting pressure, Haines jump size and interval. Reasonable agreement is observed, and impacts of grain shape are discussed. In particular, under the condition of same porosity for all studied cases, the average size of menisci is found to be smaller in porous media with angular grains, showing a tendency of pinning at narrower throats as a result of wider distribution of throat sizes (Fig. 3(B)) and greater pinning strength (Eqn. (1)).

Our results have provided direct numerical evidence of wide distribution of contact angles observed experimentally in mineralogically homogeneous porous media. The profound influences of grain shape are highlighted by systematically analyzing the displacement processes, deepening the understanding of the interplay between pore geometry and wettability. The proposed pore-network model offers an efficient approach for investigation of multiphase flow in natural porous media.

## Acknowledgments

This work was financially supported by Australian Research Council (Projects DP170102886) and The University of Sydney SOAR Fellowship. YG acknowledges the financial support of Labex MMCD(ANR-11-LABX-022-01) for his stay at Laboratoire Navier at ENPC. ZW. thanks Ms Zi Ying for fruitful discussion. Data sets associated with this work are available online (<https://doi.org/10.6084/m9.figshare.13369733>).

## References

AlRatrou, A., Blunt, M. J., & Bijeljic, B. (2018). Wettability in complex porous

- materials, the mixed-wet state, and its relationship to surface roughness. *Proceedings of the National Academy of Sciences*, 115(36), 8901–8906. doi: 10.1073/pnas.1803734115
- Armstrong, R. T., Georgiadis, A., Ott, H., Klemin, D., & Berg, S. (2014). Critical capillary number: Desaturation studied with fast x-ray computed microtomography. *Geophysical Research Letters*, 41(1), 55–60. doi: 10.1002/2013GL058075
- Blunt, M., Fayers, F., & Orr, F. M. (1993). Carbon dioxide in enhanced oil recovery. *Energy Conversion and Management*, 34(9), 1197–1204. (Proceedings of the International Energy Agency Carbon Dioxide Disposal Symposium)
- Blunt, M. J. (1998). Physically-based network modeling of multiphase flow in intermediate-wet porous media. *Journal of Petroleum Science and Engineering*, 20(3), 117–125. doi: [https://doi.org/10.1016/S0920-4105\(98\)00010-2](https://doi.org/10.1016/S0920-4105(98)00010-2)
- Blunt, M. J. (2001). Flow in porous media — pore-network models and multiphase flow. *Current Opinion in Colloid & Interface Science*, 6(3), 197–207. Retrieved from <http://www.sciencedirect.com/science/article/pii/S135902940100084X> doi: [https://doi.org/10.1016/S1359-0294\(01\)00084-X](https://doi.org/10.1016/S1359-0294(01)00084-X)
- Blunt, M. J. (2017). *Multiphase flow in permeable media: A pore-scale perspective*. Cambridge University Press. doi: 10.1017/9781316145098
- Blunt, M. J., Alhosani, A., Lin, Q., Scanziani, A., & Bijeljic, B. (2021). Determination of contact angles for three-phase flow in porous media using an energy balance. *Journal of Colloid and Interface Science*, 582, 283–290. doi: <https://doi.org/10.1016/j.jcis.2020.07.152>
- Blunt, M. J., Lin, Q., Akai, T., & Bijeljic, B. (2019). A thermodynamically consistent characterization of wettability in porous media using high-resolution imaging. *Journal of Colloid and Interface Science*, 552, 59–65. doi: <https://doi.org/10.1016/j.jcis.2019.05.026>
- Cieplak, M., & Robbins, M. O. (1988, May). Dynamical transition in quasistatic fluid invasion in porous media. *Phys. Rev. Lett.*, 60, 2042–2045. doi: 10.1103/PhysRevLett.60.2042
- Cieplak, M., & Robbins, M. O. (1990, Jun). Influence of contact angle on quasistatic fluid invasion of porous media. *Phys. Rev. B*, 41, 11508–11521. doi: 10.1103/PhysRevB.41.11508
- Furuberg, L., Måløy, K. J., & Feder, J. (1996, Jan). Intermittent behavior in slow drainage. *Phys. Rev. E*, 53, 966–977. doi: 10.1103/PhysRevE.53.966
- Geistlinger, H., & Zulficar, B. (n.d.). The impact of wettability and surface roughness on fluid displacement and capillary trapping in 2d- and 3d-porous media part 1: Wettability-controlled phase transition of trapping efficiency in glass beads packs. *Water Resources Research*, n/a(n/a), e2019WR026826. (e2019WR026826 2019WR026826) doi: 10.1029/2019WR026826
- Gibbs, J. W. (1961). *The scientific papers* (Vol. 1). New York: Dover Publications.
- Holtzman, R. (2016). Effects of pore-scale disorder on fluid displacement in partially-wettable porous media [Journal Article]. *Sci Rep*, 6, 36221. doi: 10.1038/srep36221
- Holtzman, R., & Segre, E. (2015, Oct). Wettability stabilizes fluid invasion into porous media via nonlocal, cooperative pore filling. *Phys. Rev. Lett.*, 115, 164501. doi: 10.1103/PhysRevLett.115.164501
- Hu, R., Lan, T., Wei, G.-J., & Chen, Y.-F. (2019). Phase diagram of quasi-static immiscible displacement in disordered porous media. *Journal of Fluid Mechanics*, 875, 448–475. doi: 10.1017/jfm.2019.504
- Ju, Y., Gong, W., Chang, W., & Sun, M. (2020). Effects of pore characteristics on water-oil two-phase displacement in non-homogeneous pore structures: A pore-scale lattice boltzmann model considering various fluid density ratios. *International Journal of Engineering Science*, 154, 103343. doi: <https://doi.org/10.1016/j.ijengsci.2020.103343>

- Jung, M., Brinkmann, M., Seemann, R., Hiller, T., Sanchez de La Lama, M., & Herminghaus, S. (2016, Nov). Wettability controls slow immiscible displacement through local interfacial instabilities. *Phys. Rev. Fluids*, 1, 074202. doi: 10.1103/PhysRevFluids.1.074202
- Lake, L., & of Petroleum Engineers (U.S.), S. (1986). *Fundamentals of enhanced oil recovery*. SPE.
- Lenormand, R., Touboul, E., & Zarcone, C. (1988). Numerical models and experiments on immiscible displacements in porous media [Journal Article]. *Journal of Fluid Mechanics*, 189(165-187). doi: 10.1017/s0022112088000953
- Lenormand, R., & Zarcone, C. (1989, Dec 01). Capillary fingering: Percolation and fractal dimension. *Transport in Porous Media*, 4(6), 599–612. doi: 10.1007/BF00223630
- Lipiec, J., Kuś, J., Słowińska-Jurkiewicz, A., & Nosalewicz, A. (2006). Soil porosity and water infiltration as influenced by tillage methods. *Soil and Tillage Research*, 89(2), 210 - 220. doi: <https://doi.org/10.1016/j.still.2005.07.012>
- Måløy, K. J., Furuberg, L., Feder, J., & Jøssang, T. (1992, Apr). Dynamics of slow drainage in porous media. *Phys. Rev. Lett.*, 68, 2161–2164. Retrieved from <https://link.aps.org/doi/10.1103/PhysRevLett.68.2161> doi: 10.1103/PhysRevLett.68.2161
- Matter, J. M., Stute, M., Snæbjörnsdóttir, S. Ó., Oelkers, E. H., Gislason, S. R., Aradóttir, E. S., ... Broecker, W. S. (2016). Rapid carbon mineralization for permanent disposal of anthropogenic carbon dioxide emissions. *Science*, 352(6291), 1312–1314. doi: 10.1126/science.aad8132
- Moura, M., Måløy, K. J., Flekkøy, E. G., & Toussaint, R. (2020). Intermittent dynamics of slow drainage experiments in porous media: Characterization under different boundary conditions. *Frontiers in Physics*, 7, 217. Retrieved from <https://www.frontiersin.org/article/10.3389/fphy.2019.00217> doi: 10.3389/fphy.2019.00217
- Nadim, F., Hoag, G. E., Liu, S., Carley, R. J., & Zack, P. (2000). Detection and remediation of soil and aquifer systems contaminated with petroleum products: an overview. *Journal of Petroleum Science and Engineering*, 26(1), 169 - 178.
- Oliver, J., Huh, C., & Mason, S. (1977). Resistance to spreading of liquids by sharp edges. *Journal of Colloid and Interface Science*, 59(3), 568 - 581. Retrieved from <http://www.sciencedirect.com/science/article/pii/0021979777900522> doi: [https://doi.org/10.1016/0021-9797\(77\)90052-2](https://doi.org/10.1016/0021-9797(77)90052-2)
- Primkulov, B. K., Pahlavan, A. A., Fu, X., Zhao, B., MacMinn, C. W., & Juanes, R. (2019). Signatures of fluid–fluid displacement in porous media: wettability, patterns and pressures. *Journal of Fluid Mechanics*, 875, R4. doi: 10.1017/jfm.2019.554
- Primkulov, B. K., Talman, S., Khaleghi, K., Rangriz Shokri, A., Chalaturnyk, R., Zhao, B., ... Juanes, R. (2018, Oct). Quasistatic fluid-fluid displacement in porous media: Invasion-percolation through a wetting transition. *Phys. Rev. Fluids*, 3, 104001. doi: 10.1103/PhysRevFluids.3.104001
- Rabbani, H. S., Or, D., Liu, Y., Lai, C.-Y., Lu, N. B., Datta, S. S., ... Shokri, N. (2018). Suppressing viscous fingering in structured porous media. *Proceedings of the National Academy of Sciences*, 115, 4833-4838. doi: 10.1073/pnas.1800729115
- Ran, H., Jiamin, W., Zhibing, Y., Yi-Feng, C., & Tetsu, T. (2018). Wettability and flow rate impacts on immiscible displacement: A theoretical model. *Geophysical Research Letters*, 45(7), 3077-3086. doi: 10.1002/2017GL076600
- Szulczewski, M. L., MacMinn, C. W., Herzog, H. J., & Juanes, R. (2012). Lifetime of carbon capture and storage as a climate-change mitigation technology. *Proceedings of the National Academy of Sciences*, 109(14), 5185–5189. doi: 10.1073/pnas.1115347109
- Trojer, M., Szulczewski, M. L., & Juanes, R. (2015, May). Stabilizing fluid-fluid dis-

- placements in porous media through wettability alteration. *Phys. Rev. Applied*, *3*, 054008. doi: 10.1103/PhysRevApplied.3.054008
- Wang, Z., Chauhan, K., Pereira, J.-M., & Gan, Y. (2019, Mar). Disorder characterization of porous media and its effect on fluid displacement. *Phys. Rev. Fluids*, *4*, 034305. doi: 10.1103/PhysRevFluids.4.034305
- Wang, Z., Pereira, J.-M., & Gan, Y. (2020). Effect of wetting transition during multiphase displacement in porous media. *Langmuir*, *36*(9), 2449-2458. (PMID: 32070092) doi: 10.1021/acs.langmuir.9b03780
- Wilkinson, D., & Willemsen, J. F. (1983, oct). Invasion percolation: a new form of percolation theory. *Journal of Physics A: Mathematical and General*, *16*(14), 3365-3376. Retrieved from <https://doi.org/10.1088%2F0305-4470%2F16%2F14%2F028> doi: 10.1088/0305-4470/16/14/028
- Xu, W., Ok, J. T., Xiao, F., Neeves, K. B., & Yin, X. (2014). Effect of pore geometry and interfacial tension on water-oil displacement efficiency in oil-wet microfluidic porous media analogs. *Physics of Fluids*, *26*(9), 093102. doi: 10.1063/1.4894071
- Yortsos, Y. C., Xu, B., & Salin, D. (1997, Dec). Phase diagram of fully developed drainage in porous media. *Phys. Rev. Lett.*, *79*, 4581-4584. doi: 10.1103/PhysRevLett.79.4581
- Zhao, B., MacMinn, C. W., & Juanes, R. (2016). Wettability control on multiphase flow in patterned microfluidics. *Proceedings of the National Academy of Sciences*, *113*(37), 10251-10256. doi: 10.1073/pnas.1603387113
- Zulfiqar, B., Vogel, H., Ding, Y., Golmohammadi, S., Küchler, M., Reuter, D., & Geistlinger, H. (n.d.). The impact of wettability and surface roughness on fluid displacement and capillary trapping in 2d- and 3d-porous media: Part 2: Combined effect of wettability, surface roughness, and pore space structure on trapping efficiency in sand packs and micromodels. *Water Resources Research*, *n/a*(n/a), e2020WR027965. (e2020WR027965 2020WR027965) doi: 10.1029/2020WR027965